

## A highly ionized stellar bow shock in the Small Magellanic Cloud

WILLIAM J. HENNEY, S. JANE ARTHUR, AND M. VALERDI<sup>1</sup>

<sup>1</sup>*Instituto de Radioastronomía y Astrofísica, Universidad Nacional Autónoma de México, Apartado Postal 3-72, 58090 Morelia, Michoacán, Mexico*

### Abstract

We report the discovery of a parsec-scale stellar bow shock associated with the O2 III(f) star Walborn 3 in the cluster NGC 346 of the Small Magellanic Cloud. Emission line images of He II and [Ar IV], etc.

**Keywords:** Atomic physics; Circumstellar matter; Stars: winds, outflows

### 1. INTRODUCTION

The interaction of a star’s wind with the surrounding medium can result in an arc-shaped circumstellar emission nebula, frequently referred to as a bow shock (Gull & Sofia 1979; van Buren & McCray 1988). Stellar bow shocks are found around a wide variety of different stars, including pre-main sequence stars (Bally & Reipurth 2001; Henney et al. 2013), neutron stars (Cordes et al. 1993), and cool giants and supergiants (Sahai & Chronopoulos 2010; Cox et al. 2012), but they are most commonly associated with hot luminous OB stars (van Buren et al. 1995; Kobulnicky et al. 2016). Bow shocks are most frequently observed via their infrared continuum emission (Meyer et al. 2016), which arises from dust grains that are heated by the stellar radiation field (Draine & Li 2007), but specific classes of bow shock have also been identified via multiple thermal and non-thermal emission mechanisms that trace gas and plasma components. The emission arcs are most commonly interpreted as due to the hydrodynamic interaction induced by supersonic relative motion of the star with respect to the ambient material (Wilkin 1996), but models involving a subsonic interaction have also been proposed (Mackey et al. 2015). Also, the role of the stellar wind ram pressure in supporting the arc may be replaced by radiation pressure in some cases, see Henney & Arthur (2019a,b,c).

Stellar bow shocks can be used to estimate stellar wind mass loss rates by applying momentum-balance arguments (Gvaramadze et al. 2012; Kobulnicky et al. 2018, 2019; Henney & Arthur 2019c). These provide an important check on more traditional spectroscopic methods (Hillier 2020), since the systematic uncertainties and biases are different. Line-driven wind theory for hot stars predicts that momentum-loss

rates should increase with metallicity,  $Z$ , as  $\dot{M}V_w \propto Z^n$  with  $n = 0.6\text{--}0.8$  (Vink et al. 2001; Vink & Sander 2021; Björklund et al. 2021) for the most luminous stars ( $L > 10^6 L_\odot$ ).

In the Milky Way, OB stellar bow shocks can be divided into two classes: *runaways* (Blaauw 1961) and *weathervanes* (Povich et al. 2008). The former have supersonic space velocities due to ejection from a binary system or stellar cluster (Hoogerwerf et al. 2001; Renzo et al. 2019), while the latter have low space velocities and are interacting with streaming motions of the local interstellar medium, such as champagne flows (Tenorio-Tagle 1979).

### 2. OBSERVATIONS

Apart from the inner rim of the bow shock, there is no diffuse He II emission in the core of NGC 346, or in the western side of the N66 region. The eastern side of N66, on the other hand, shows extensive He II  $\lambda 4686$  emission, as can be seen at offsets from  $-200$  to  $-50$  arcsec in Figure 5b. The eastern side of N66 also shows a ten times higher [Fe III] /  $H\beta$  ratio and disturbed kinematics in low-ionization lines such as [S II]. All these are probably due to a foreground supernova remnant SNR B0057–72.2 (Ye et al. 1991) that overlaps with this part of the nebula (Chu & Kennicutt 1988; Nazé et al. 2002; Danforth et al. 2003).

### 3. RESULTS

### 4. CONCLUSIONS

1 Thank you.

*Facilities:* VLT:Yepun (MUSE)

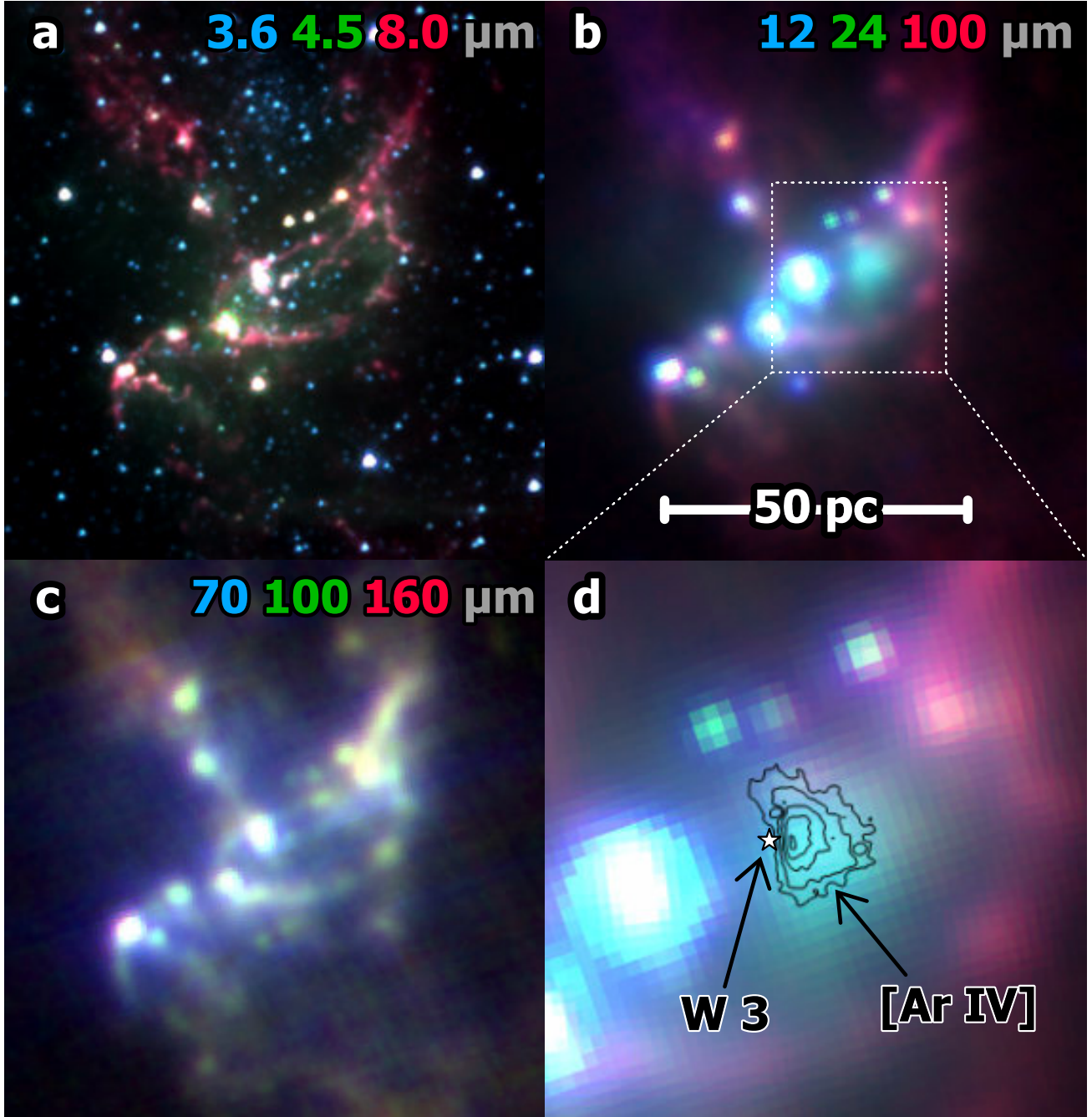


**Figure 1.** Panoramic view of the NGC 346/N66 region at infrared wavelengths: (a) Short wavelength mid-infrared (3.6 to 8  $\mu\text{m}$ ); (b) Longer wavelength mid-infrared (12 to 100  $\mu\text{m}$ ); (c) Far-infrared (70 to 150  $\mu\text{m}$ ); (d) Zoomed view of panel c. Images are from satellite observatories as follows: *Spitzer* IRAC 3.6, 4.5, 8  $\mu\text{m}$ ; *WISE* 12  $\mu\text{m}$ ; *Spitzer* MIPS 24, 70  $\mu\text{m}$ ; *Herschel* PACS 100, 150  $\mu\text{m}$ .

#### REFERENCES

- |  |   |
|--|---|
| Bally, J., & Reipurth, B. 2001, <i>ApJ</i> , 546, 299                                    | Cordes, J. M., Romani, R. W., & Lundgren, S. C. 1993, <i>Nature</i> , 362, 133          |
| Björklund, R., Sundqvist, J. O., Puls, J., & Najarro, F. 2021, <i>A&amp;A</i> , 648, A36 | Cox, N. L. J., Kerschbaum, F., van Marle, A.-J., et al. 2012, <i>A&amp;A</i> , 537, A35 |
| Blaauw, A. 1961, <i>BAN</i> , 15, 265  |   |
| Chu, Y.-H., & Kennicutt, Robert C., J. 1988, <i>AJ</i> , 95, 1111                        |   |

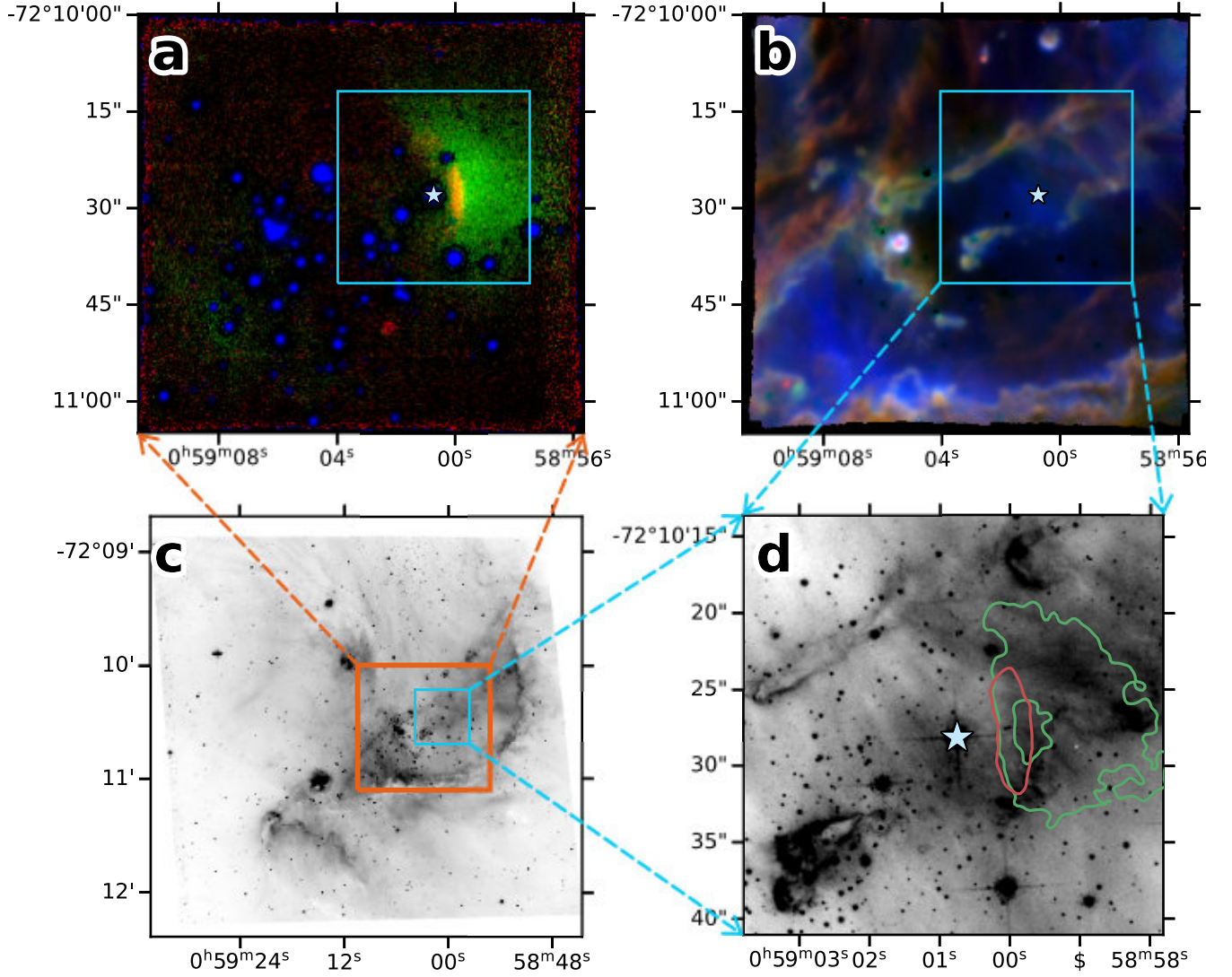


**Figure 2.** MUSE emission line images of the core of NGC 346. (a) High-ionization emission from the bow shock. (b) Medium to low-ionization emission from the surrounding H II region. (c) Location of the MUSE field within the wider nebula. (d) Zoom on the bow shock region in the light of H $\alpha$  emission.

Danforth, C. W., Sankrit, R., Blair, W. P., Howk, J. C., & Chu, Y.-H. 2003, *ApJ*, 586, 1179  
 Draine, B. T., & Li, A. 2007, *ApJ*, 657, 810  
 Gull, T. R., & Sofia, S. 1979, *ApJ*, 230, 782  
 Gvaramadze, V. V., Langer, N., & Mackey, J. 2012, *MNRAS*, 427, L50  
 Henney, W. J., & Arthur, S. J. 2019a, *MNRAS*, 486, 3423  
 —. 2019b, *MNRAS*, 486, 4423  
 —. 2019c, *MNRAS*, 489, 2142  
 Henney, W. J., García-Díaz, M. T., O’Dell, C. R., & Rubin, R. H. 2013, *MNRAS*, 428, 691  
 Hillier, D. J. 2020, *Galaxies*, 8, 60  
 Hoogerwerf, R., de Bruijne, J. H. J., & de Zeeuw, P. T. 2001, *A&A*, 365, 49

Kobulnicky, H. A., Chick, W. T., & Povich, M. S. 2018, *ApJ*, 856, 74 (K18)  
 —. 2019, *AJ*, 158, 73  
 Kobulnicky, H. A., Chick, W. T., Schurhammer, D. P., et al. 2016, *ApJS*, 227, 18  
 Mackey, J., Gvaramadze, V. V., Mohamed, S., & Langer, N. 2015, *A&A*, 573, A10  
 Meyer, D. M.-A., van Marle, A.-J., Kuiper, R., & Kley, W. 2016, *MNRAS*, 459, 1146  
 Nazé, Y., Hartwell, J. M., Stevens, I. R., et al. 2002, *ApJ*, 580, 225  
 Povich, M. S., Benjamin, R. A., Whitney, B. A., et al. 2008, *ApJ*, 689, 242  
 Renzo, M., Zapartas, E., de Mink, S. E., et al. 2019, *A&A*, 624, A66

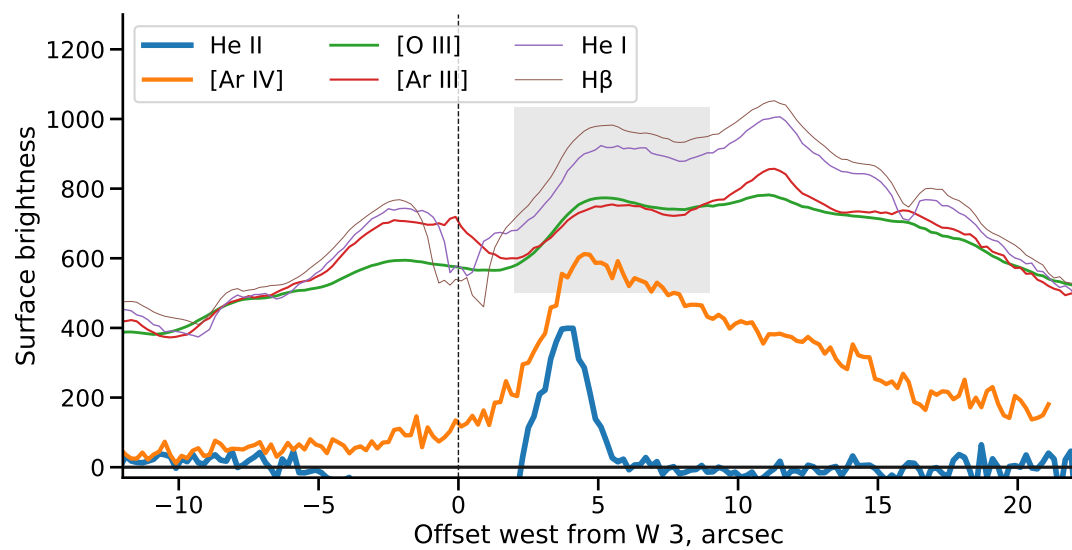


**Figure 3.** Emission line surface brightness profiles along an East–West cut across the bow shock, derived from MUSE integral field spectra.

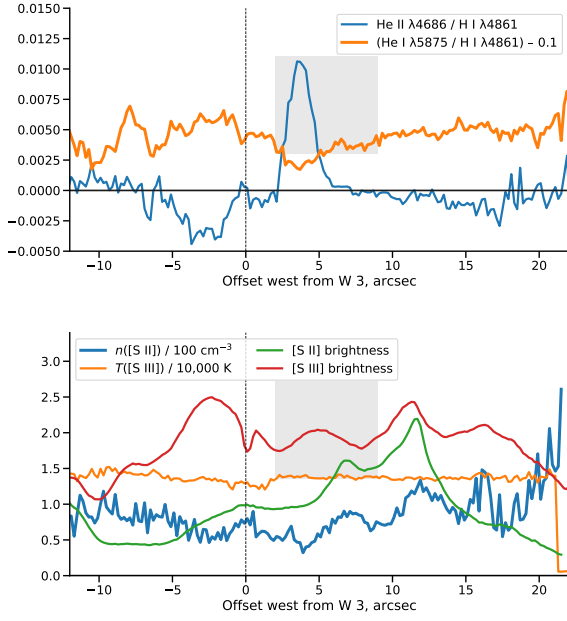


**Figure 4.** More profiles

Sahai, R., & Chronopoulos, C. K. 2010, ApJL, 711, L53

Tenorio-Tagle, G. 1979, A&A, 71, 59

van Buren, D., & McCray, R. 1988, ApJL, 329, L93

van Buren, D., Noriega-Crespo, A., & Dgani, R. 1995, AJ, 110, 2914

Vink, J. S., de Koter, A., & Lamers, H. J. G. L. M. 2001, A&A, 369, 574

Vink, J. S., & Sander, A. A. C. 2021, MNRAS, 504, 2051

Wilkin, F. P. 1996, ApJL, 459, L31

Ye, T., Turtle, A. J., & Kennicutt, R. C., J. 1991, MNRAS, 249, 722

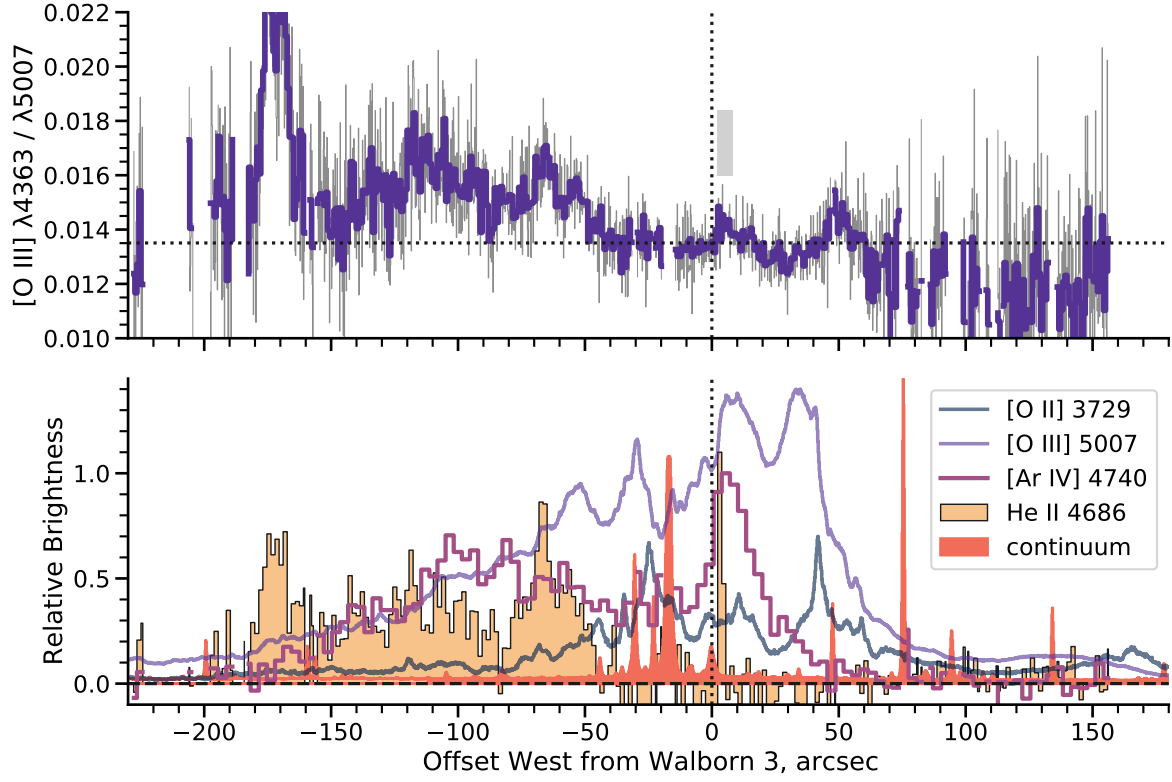


**Figure 5.** Emission line surface brightness profiles and line ratios along a large-scale East–West cut across the entire region, based on FORS1 longslit spectra. The slit is close to the symmetry axis of the bow shock. (a) Temperature-sensitive line ratio [O III] 4363/5007. The gray box shows the same inner rim region of the bow shock that is highlighted by a gray box in Fig. 3. (b) Selected emission lines from a wide range of ionization stages.

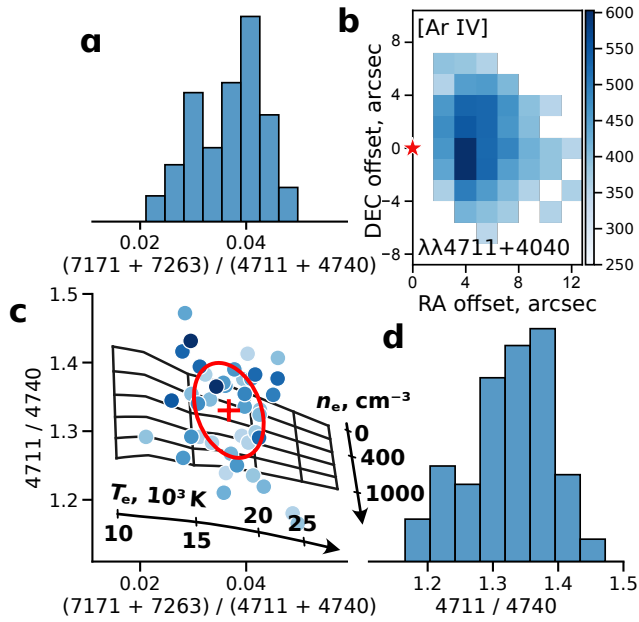


**Figure 6.** Temperature and density diagnostics of the bow shock from [Ar IV] line ratios.



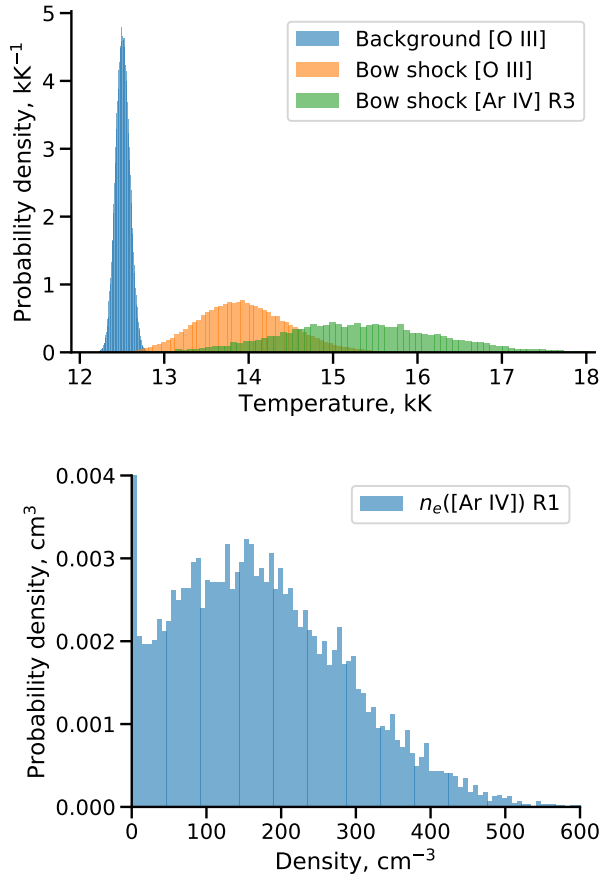


**Figure 7.** Derived temperature of nebula and bow shock.